DOI: 10.1113/EP087551

Non-invasive prediction of Genotype-positive/Phenotype negative in Hypertrophic Cardiomyopathy by 3D Modern Shape Analysis

Paolo Piras PhD[1*], Concetta Torromeo, MD[1], Antonietta Evangelista MD PhD[2], Giuseppe Esposito MD[1], Paola Nardinocchi PhD[3], Luciano Teresi PhD[4], Andrea Madeo MD[5], Federica Re MD[5], Claudia Chialastri MD PhD[5], Michele Schiariti MD[1], Valerio Varano PhD[6], Paolo Emilio Puddu MD PhD[1]

[1]Dept. Scienze Cardiovascolari, Respiratorie, Nefrologiche, Anestesiologiche e Geriatriche, Sapienza, Università di Roma, 0161, Italy.

[2]Ospedale San Giovanni Calibita Fatebenefratelli Isola Tiberina, Rome, 00186, Italy.

[3]Dept. Structural engineering & geotechnics, Sapienza Università di Roma, Rome, 00161, Italy.

[4]Dept. Mathematics & Physics, Roma Tre University, Rome, 00146, Italy.

[5]Ospedale San Camillo-Forlanini, Rome, 00152, Italy.

[6]Dept. Architecture, Roma Tre University, Rome, 00146, Italy.

Correspondence: **ppiras@uniroma3.it**

Abstract

We propose a noninvasive procedure for predicting genotype positive for hypertrophic cardiomyopathy (HCM) in subjects that do not exhibit a left-ventricular wall hypertrophy condition (G+LVH-); the procedure is based on the enhanced analysis of medical imaging from 3D speckle tracking echocardiography (3D STE). 3D STE, due to its low quality images has not been used so far to detect effectively the G+LVH- condition. Here, we post-process Echocardiographic images exploiting the tools of modern shape analysis, and we study the motion of the left ventricle (LV) during an entire cycle. We enrolled 82 Controls, 21 HCM patients, and 11 G+LVH- subjects. We follow two steps:i) we select the most impaired regions of LV by analyzing its strains; ii) we use shape analysis on these regions to classify the subjects. The G+LVH- subjects show different trajectories and deformational attributes. We found high classification performance in terms of AUC (~90), sensitivity (~78) and specificity (~79). Our results show that i) G+LVH- present

important deformational impairments relative to healthy controls and that ii) modern shape analysis can efficiently predict genotype by means of a noninvasive and not expensive technique such as 3DSTE.

KEYWORDS

3D Echocardiography, Modern Shape Analysis, Genetics, Hypertrophic Cardiomyopathy, Genotype positive.

1. NEW FINDINGS

What is the central question of this study? The aim was to determine impaired deformational indicators for G+LVH- in Hypertrophic Cardiomyopathy using non-invasive 3D echocardiography.

What are the main findings and its importance? Our results indicate that, using 3DSTE and modern shape analysis, peculiar deformational impairments can be detected in G+LVH- and that they can be classified with good accuracy. Moreover, the patterns of impairment are located mainly on the apical region in agreement with other evidence coming from previous bio-mechanical investigations.

2. INTRODUCTION

Hypertrophic cardiomyopathy (HCM) is the most common genetically determined cardiac disease; more than 1400 mutations affecting about 13 genes have been identified (Maron & Maron, 2013). In the last two decades, HCM has been considered mainly an autosomal dominant disease albeit some cases are explained by new mutations, and less commonly, autosomal recessive inheritance. Thus, these mutations may have incomplete expression with a variable phenotype and age-related expression (Maron, Ommen, Semsarian, Spirito, Olivotto, & Maron, 2014). The first degree relatives of HCM subjects have approximately a 50% probability of genetic carriage. HCM presents also a peculiar subclinical condition: the presence of gene mutation without left ventricle (LV) hypertrophy, a condition called penotype positive/ LVH- (G+LVH-) (Maron, & Semsarian, 2010; Maron, Yeates, & Semsarian, 2011; Gray, Ingles, & Semsarian, 2011).

For HCM patients texture analysis was also used (Schofield et al., 2016; Baeßler, Mannil, Maintz, Alkadhi, & Manka, 2018) showing that HCM condition presents different texture image features relatively to Controls. Recently, some efforts have been done to look for phenotypic indicators able to predict (e.g. classify) the G+LVH- condition. 2D and 3D speckle tracking echocardiography (2D STE and 3D STE) were also used (Yiu et al., 2012). It was found that in G+LVH- untwist and unstrain (=strain reduction during diastolic phase) are delayed and untwist rate and unstrain rate are decreased (Kauer et al., 2017). Others found no significant differences in deformation, using global or regional (e.g. American heart association [AHA] segments) strains

of both left atrium (LA) or LV (Aly, Brouwer, Kleijn, van Rossum & Kamp, 2014). De et al. (2016) do not support previous reports regarding the presence of subclinical echocardiographic abnormalities found in G+LVH-, whereby a higher global peak late diastolic annular velocity was found. However, by echocardiography few deformational impairments were able to classify accurately G+LVH- (Haland et al., 2017).

Good accuracy to classify G+LVH- was obtained by cardiac magnetic resonance (CMR) using the presence of myocardial crypts, anterior mitral valve leaflet length, increased LV apical trabecular complexity (measured via fractal dimension) and smaller LV systolic cavity (Captur et al., 2014a,b; Maron et al., 2012). It is important to underline that while CMR is a more expensive investigation with respect to echocardiography, 3D STE is definitely easier to access and obtain.

The cost of diagnostic genetic testing, although decreased more recently, should be compared with those of a tool that might predict genotype non-invasively. In this context, we propose here a new translational approach evolved from previous research (Piras et al., 2016; Piras et al., 2017a,b; Varano et al., 2017).

Looking for new pre-clinical indicators of G+LVH-, we couple standard 3D STE analysis with modern shape analysis (i.e. geometric morphometrics, GM) and 4D analysis of LV trajectory. Geometric Morphometrics proved to be an effective tool for shape analysis in a very wide spectrum of disciplines from paleobiology to zoology to medicine (Piras et al., 2009; Piras et al., 2014; Maiorino et al., 2013; Madeo et al., 2015). Although we have previously shown (Madeo et al., 2015) that HCM patients present important LV deformational impairments, it is clear that the pretest probability related to these impairments is much smaller; thus, it is required the search for more subtle abnormalities, at a smaller length scale. With the aim of gauging local deformations, we compute strain data using the full landmark's sampling coming from the 3D echocardiography; these local strains are then represented by a bull's-eye plot, superimposed on the classic 16 or 17 LV segments indicated by the AHA.

Fig.1, top, shows the full set of landmarks tracked by the 3D echocardiography; panel (A) shows the actual geometry of the LV, while panel (B) uses a bullseye plot to show the position of the landmarks with respect to the AHA segments. The two bull's-eye plots of Fig. 1, bottom, show the mean radial strain in each sector (left) and the local radial strain (right); this example clearly shows that the region with maximum strain (identified by dotted lines) is localized between two segments, a finding which cannot be inferred from the bullseye plot at left.

Our working hypothesis is that actual differences between cohorts could be biased by the use of segment-wise mean values, resulting in an ineffective search for group dissimilarities, and their consequent classification. In this paper we combine the ne computation of 3D STE strains and rotational parameters with the potential of shape analysis in order to identify and classify G+LVH- carriers on a sample comprising healthy Control subjects, HCM and G+LVH- individuals. We demonstrate the full prospective of modern shape analysis applied to a relatively easy and cost-reduced examination (i.e. 3D STE) and its ability in identifying with very good accuracy G+LVH- genetic condition.

3. MATERIALS AND METHODS

1. Ethical approval

Informed consent was obtained from each subject under study. This study conformed to the standards set by the latest revision of the Declaration of Helsinki and the procedure as approved by the Ethical Committee of Policlinico Umberto I, the central Hospital of the the Dipartimento di Scienze Cardiovascolari, Respiratorie, Nefrologiche, Anestesiologiche e Geriatriche, Sapienza Università di Roma (reference number: 2655; protocol number 39/13). This study was not registered in a database.

2. Study population

Following Madeo el al. (2015), Piras et al. (2016), Piras et al. (2017b), Varano et al. (2017), we acquired data using PST-25SX Artida device, Toshiba Medical Systems Corp., Tokyo, Japan. 114 consecutive subjects underwent 3D STE acquisition; control (n=82), G+LVH- (n=11) and HCM (n=21) categories were represented.

Inclusion criteria for HCM patients were determined by a LV wall thickness ≥ 13 mm. Table 1 reports details and descriptive statistics for the population under study; the 21 HCM, plus the 11 G+LV- patients belong to 10 families.

Members of HCM families with pathogenic sarcomere mutations were potential participants, focusing on G+LVH- mutation carriers. G+LVH- subjects were eligible for inclusion in this study if they (1) were confirmed to carry their family's pathogenic or likely pathogenic HCM-associated sarcomere mutation (G+); (2) did not have echocardiographic evidence of hypertrophy (LVH-) defined as maximal LV wall thickness ≤ 12mm. G+ individuals were defined if carrying a mutation in one or more of these sarcomeric genes: myosin-binding protein C (MYBPC3), β -myosin heavy chain (MYH7), troponin T (TNNT2), troponin I (TNNI3), myosin regulatory light chain (MYL2), myosin essential light chain (MYL3), tropomyosin (TPM1), and cardiac α -actin (ACTC1).

1. Thick-filament mutations: MYBPC3, MYH7, MYL2, and MYL3
2. Thin-filament mutations: TNNT2, TNNI3, TPM1, and ACTC1.

The pathogenicity of sarcomere variants was determined using standard criteria as previously described in published genetic methodologies (Prabhakar et al., 2001).

Genomic DNA was extracted from peripheral blood according to QIAamp DNA Blood BioRobot MDx kit (QIAGEN GmbH, Hilden, Germany). In vitro amplification of all candidate exons was performed by polymerase chain reaction using primers described previously (Torricelli et al., 2003; Xiao & Oefner, 2001;

Yu et al., 2005). These HCM susceptibility genes are the basis of commercially available genetic tests for HCM (for a comprehensive list of mutations and polymorphisms in sarcomere protein genes associated with HCM, see ; for genetic tests, see http://www .correlagen.com).

Sequence variations were detected by denaturing high-performance liquid chromatography (DHPLC) using the WAVE DNA Fragment Analysis System (Transgenomics, San Jose, CA). The conditions for DHPLC were developed on the basis of exon specific melting profiles predicted by NAVIGATOR software (Transgenomic, Omaha, NE). Abnormal DHPLC elution pro les were sequenced on automated dye terminator cycle sequencing using an ABI Prism 3100 Genetic Analyzer (Applied Biosystems, Foster City, KS). Every mutation identified was confirmed by a new polymerase chain reaction, and, when possible, by restriction enzyme digestion. We excluded other causes of LV hypertrophy in selecting HCM patients. Table 2 reports details about genetic mutations carried by subject under study.

TABLE 1. Summary statistics ± Standard Deviation for the population under study; in each entry *n* indicates actual sample size thus excluding case-wise missing cases. We report ejection fraction computed using both 2D and 3D reconstructions.

	Control N=82		**G+LVH- N=11**		**HCM N=21**	
Sex (M/F)	48/34	n=82	3/8	n=11	14/7	n=21
	Mean ± sd	**n**	**Mean ± sd**	**n**	**Mean ± sd**	**n**
Age (years)	38.53 ± 7.88	n=81	40.46 ± 13.5	n=11	47.76 ± 12.88	n=21
EF-Two-dim (%)	60.36 ± 5.1	n=66	61.09 ± 6.8	n=11	62.06 ± 9.9	n=16
EF-Three-dim (%)	57.12 ± 5.6	n=82	50.20 ± 11.3	n=11	53.70± 7.73	n=21
Weight (Kg)	71.41 ± 12.27	n=66	72 ± 13.41	n=7	74.6 ± 14.58	n=20
BSA (m2)	1.84 ± 0.19	n=66	1.76 ± 0.17	n=11	1.86 ± 0.16	n=19
BMI (Kg/m2)	23.91 ± 3.09	n=66	25.99 ± 4.57	n=7	25.38 ± 3.9 8	n=20
IVS (mm)	8.20 ± 1.45	n=66	9.46 ± 1.57	n=11	18.09 ± 3.96	n=21
SBP (mm Hg)	116.41 ± 9.61	n=64	120 ± 7.75	n= 11	121.5 ± 10.27	n=20
DBP (mmHg)	73.98 ± 7.72	n= 64	74.55 ± 6.88	n= 11	77 ± 8.18	n= 20
Genetic Mutations						
MYBPC3			8		11	

MYH7			1	9
TNNT2			2	1

TABLE 2. Details about Amino acid and nucleotidic substitution.

Anonymized individual code	Condition	Gene	Amino Acid change	DNA sequence change
368	G+LVH-	*MYBPC3*	p.Gln205Ter	c.613C>T
250	HCM	*TNNT2*	p.Arg84Thr	c.251G>C
252	G+LVH-	*TNNT2*	p.Arg84Thr	c.251G>C
281	HCM	*MYBPC3*	p.Met555Thr	c.1664T>C
330	G+LVH-	*MYBPC3*	p.Met555Thr	c.1664T>C
331	G+LVH-	*MYBPC3*	p.Met555Thr	c.1664T>C
341	G+LVH-	*MYBPC3*	p.Met555Thr	c.1664T>C
276	HCM	*MYH7*	p.Arg652Gly	c.1954A>G
173	HCM	*MYBPC3*	p.Gln1259*	c.3775C>T
148	G+LVH-	*MYBPC3*	p.Gln1259*	c.2309-2A>G
149	HCM	*MYBPC3*	p.Gln1259*	c.2309-2A>G
372	G+LVH-	*MYH7*	p.Arg652Gly	c.1954A>G
305	HCM	*MYBPC3*	p.Met555Thr	c.1664T>C
301	HCM	*MYH7*	p.Glu1116Lys	c.3346G>A
170	HCM	*MYBPC3*	p.Gln1259*	c.1664T>C
232	HCM	*MYBPC3*	p.Gln1259*	c.1664T>C
241	HCM	*MYBPC3*	p.Gln1259*	c.1664T>C
370	G+LVH-	*MYBPC3*	p.Gln1259*	c.1664T>C
371	G+LVH-	*MYBPC3*	p.Gln1259*	c.1664T>C
253	G+LVH-	*TNNT2*	p.Arg84Thr	c.251G>C
304	HCM	*MYH7*	p.Arg143Gln	c.428G>A
191	HCM	*MYH7*	p.Leu517Met	c.1549C>A
192	HCM	*MYH7*	p.Leu517Met	c.1549C>A
193	HCM	*MYH7*	p.Leu517Met	c.1549C>A
194	HCM	*MYH7*	p.Leu517Met	c.1549C>A
300	HCM	*MYH7*	p.Asn160=	c.480C>T
367	HCM	*MYBPC3*	Mis-splicing	c.2309-2A>G
284	HCM	*MYH7*	p.Ala797Thr	c.2389G>A
329	G+LVH-	*MYBPC3*	p.Gln1259*	c.1664T>C
302	HCM	*MYBPC3*	p.Gln969Ter	c.2905C>T
282	HCM	*MYBPC3*	p.Gly1206Asp	c.1664T>C
283	HCM	*MYBPC3*	p.Gly1206Asp	c.1664T>C

1. Raw data from 3D echocardiography

The raw data consist of a sequence of geometries for each subject, representing the shapes of the LV during the cardiac revolution. The LV geometries for each subject are reconstructed starting from 6 homologous landmarks, manually identified by the operator while browsing the diastolic frame; always the same operator (AE) was involved in LV reconstruction. Each geometry is sampled by a set of landmarks for each of the endocardial and epicardial layers; in particular, each of the two LV layers is sampled by 1297 landmarks in total; the Artida device considers 36 cross sections along the axis base-apex, and tracks the position of 36 landmarks for each section, plus the position of the apex. By using the device, it is possible to post process directly the data of each subject, so to compute the mean values of some motion parameters, such as rotation, torsion and other strain measures.

Our group is using an unlocked version of the software equipping the PST-25SX Artida device, and has access to the raw data, that is, to the coordinates of all the landmarks acquired. It is important to note that our findings are based on the usage of the these raw data. This special opportunity has been possible thanks to an official re- search and development agreement between the Dipartimento di Scienze Cardiovascolari, Respiratorie, Nefrologiche Anestesiologiche e Geriatriche, Sapienza-Università di Roma and Toshiba Medical System Europe, Zoetermeer, NL.

2. Reconstructed dataset at homologous times

The reconstructed dataset consists of a sequence of geometries for each subject, extracted from the raw data at homologous times. The 3D Artida device acquires data using at approximately constant time-rate ($\sim$ 40ms), which yields a different number of time frames for each subject, depending on the individual heart cycle duration.

In order to study trajectory attributes, it is essential to perform shape analysis using shapes which correspond to physiologically homologous times; thus, we decided to extract 16 shapes from the raw data (which may contain more time frames) as follows. At first, we focus on 4 primal times, as shown in Fig.2: two mechanical, LV end-systole and mitral valve opening, and two electrical, R wave peak and P wave peak. For each subject, the time value (in milliseconds) of these 4 primal times is manually recorded by carefully browsing the 3D STE video clip to detect the aforementioned events. It follows that the primal times are strictly homologous among the subjects.

Then, between two consecutive primal times, we consider three additional, equally-spaced, times, yielding a total of 16 homologous times. Using these times, we reconstruct the corresponding 16 geometries via a cubic

spline interpolation of raw data. All in all, the resulting dataset is constituted by 16 shapes, each composed by 2594 landmarks (1297 for both the epicardium and the endocardium), for each of the 114 subjects under study.

3. 3D STE for landmark selection

In the following post processing, we always used our reconstructed dataset. The goal of this step is the selection of the landmarks whose motion is more influenced by the pathology. To this aim, we assumed the diastole as reference configuration, and we computed Radial, Circumferential and Longitudinal strains, as well as Rotation, of the systolic configuration with respect to the diastole for each landmark in the configuration. Then, to assess the systo-diastolic differences, we performed individual, landmark-wise, ANOVAs for the four parameters.

We selected the landmarks having at least one of the four parameters significant under ANOVA with Control/G+LVH- as two-levels factor variable, and with an absolute value of Cohen'd effect size > 1; this threshold could appear arbitrary, but actually it can be considered rather restrictive in selecting specific locations as the value of 0.8 is traditionally considered "large" in statistical literature (Sawilowsky, 2001). HCM was not used in this step as our purpose is to distinguish G+LVH- from Controls. HCM were then included in successive analyses of the selected landmarks.

3. EXPERIMENTS

1. Modern shape analysis

In the following, we always used the selected landmarks as input data for shape analysis. In particular, modern shape analysis has been performed according to the following algorithm:

1. We use the Shape Space, by scaling all shapes at the same size, gauged by their centroid size, see Madeo et al. (2015).
2. We compute the grand mean using the whole data, that is, all the shapes of all the subjects;
3. For each subject, we compute the local mean, and then the deformation of each shape of the cycle (at the 16 homologous times) with respect to the local mean; we note that here diastole is treated as a deformed state, in contrast to what happens in classic 3D STE analysis where diastole is assumed as reference.

4. For each subject, we transport the previously computed deformation toward the gran mean; for this very important step we used the Parallel Transport technique via Linear Shift (Piras et al., 2016; Piras et al., 2017a; Varano et al., 2017).

5. The transported deformations are eventually used to generate a sequence of shapes in the neighborhood of the gran mean: for each subject, there is a one-to-one correspondence between the original shapes of a cycle, and the shapes transported around the gran mean. It is worth noting that these steps are essential to filter out initial inter-individual differences of shapes;

Finally, we performed a Generalized Procrustes Analysis in the Shape Space, followed by a Principal Component . Any difference gauged during this step represents changes in deformation (that is, in motion) rather than in shape. The same sequence was successfully used in (Piras et al., 2016; Piras et al., 2017a; Varano et al., 2017).

We conclude by noting that including the HCM category allows to orient the axes of shape variation so that the three categories (Control, G+LVH-, HCM) are in the same ordination space. The algorithm to evaluate orientation, size and shape of the LV trajectories is presented in Piras et al. (2017b).

1. Machine learning for G+LVH- classification

One of the most used techniques in machine learning is support vector machine (SVM). It was successfully applied to data similar to those treated here in Piras et al. (2017b). We used the first 6 PC scores evaluated at all homologous times for a total of 96 predictors. Preliminarily, we proceeded for an univariate features selection: we computed univariate ANOVAs between Control and G+LVH- for each predictor. All those predictors having significant ANOVA (at 0.05 significance level) and with an absolute Cohen'd effect size > 1 were retained for SVM. We adopted here a permutated version of SVM on split data Piras et al. (2017a).

Controls and G+LVH- are unbalanced (i.e. 82 vs. 11 individuals); for this reason we chose to randomly select, as training dataset, the same number of individuals from the designated predictors, e.g. 8 Controls and 8 G+LVH- that are used for learning. The remaining test dataset of 74 Controls and 3 G+LVH- is then classified ex novo using the support vectors extracted during the learning procedure. This was repeated 1000 times, recording mean and median ROC'AUC, sensitivity, specificity and total accuracy from the 1000 simulated values. We also tested the normality of these 1000 simulated values for each quantity using the Lilliefors test and we anticipate that they all deviate from normality. Thus, we computed the 95% confidence intervals of the medians for the simulated distributions using bootstrap resampling.

We note that for G+LVH- there exists a certain amount of redundancy in permutations, as the maximum number of combinations of 8 out of 11 is 165; on the other side, for Controls the maximum number of combinations of 8 out of 82 is of the order of 1e13. It turns out that any sample of 8 HCM plus 8 G+LVH- of the 1000 randomizations can be considered confidently unique and not redundant with each other.

In order to test for the stability of this machine learning, we repeated the entire procedure at three very different values of SVM hyperparameter C (0.1, 25, 100), i.e. the cost of classification. A large C gives low bias and high variance, that is, the cost of misclassification is highly penalized; a small C gives higher bias and lower variance. For the parameter γ (also called σ) we used the automatic optimization implemented in the function *sigest()* of the "kernlab" R package (Karatzoglou, Smola, Hornik & Zeileis, 2004).

2. Reproducibility

We focus on the reproducibility of the reconstruction rather than on acquisition + reconstruction pipeline. In particular, one clip for each subject has been acquired, then it has been used several times to reconstruct many replicas, thus testing reconstruction' reproducibility.

As the same operator (AE) was involved in geometry reconstructions, we performed an intra-observer reproducibility analysis. The LV of 7 Controls and 3 HCM patients (all of them randomly chosen) were reconstructed twice at a temporal distance larger than one year (long-term). We computed the coefficient of variation of standard 3D-STE global strains and volumes of LV, using not only the systolic values but also those corresponding to all the frames acquired by the device during one cycle.

Then, as we propose here some novel indicators built using the GM paradigm, we applied to each replica's couple of acquisitions the deformation analysis presented above. We then evaluated the shape distance, via Procrustes distance, between the shapes of the cycles (using the first three PC scores as explained above) of each replica of the same subject parameterized on the maximum value it can assume on the tangent space that is pi/2. Coefficient of variation in percentage (i.e. standard deviation divided by the mean x 100) applied to absolute difference between the two replicas of each subject for the global 3D STE parameters was used to assess the reproducibility of classical 3D STE variables. Tentatively, one of us (GE) digitized the same subjects used for intra-observer reproducibility twice at a temporal distance of one day (short-term). These data were used for the assessment of inter-observer variability.

6. RESULTS

1. Reproducibility

Intra-observer variability analysis shows that the reproducibility of our results is always very high, as the coefficient of variation is smaller than 2% on average. Traditional global 3D STE parameters of the LV show a very good coefficient of variation; global values are: Volume: 1.56%; Radial Strain: 0.84%; Circumferential Strain: 0.79%; Longitudinal Strain: 0.81%; Rotation: 1.18%; Twist: 0.96%; Torsion Regional: 0.84%; Torsion Basal: 0.96%; Strain 3D: 0.79%; Radial Displacement 0.64%; Longitudinal Displacement 1%. The same emerges from the distances between the shape of cycle replicas of the same subject parameterized on pi/2: mean: 0.00991±0.01605. Inter-observer variability returned also a very good performance being coefficient of variation of traditional global 3D STE parameters of the left ventricle always smaller than 5%.

2. 3D STE used for selecting landmarks

Endocardium presented the strongest signal in separating Control from G+LVH- according to the 3D strain and rotation. All following results are relative to the analyses performed on this layer. Landmarks sub-selection procedure identified 400 endocardial landmarks used for shape analysis. Fig. 3 shows bull's-eye representation of the four above mentioned 3D STE parameters evaluated at systolic state. Only selected landmarks are depicted while the others have been shut off.

For sake of visualization we interpolated the white space between landmarks on the bullseye circular domain using kriging geostatistical technique. They are located mainly in the apical and mid parts of the LV while a small group of landmarks is located in the basal-septal segment. This visualization allows i) to locate immediately the position of landmarks selected under each parameter, ii) to appreciate the intensity of the parameter on the mean of Control sample (n=82) and iii) to evaluate the effect size, including its sign, associated to each landmark on the two categories. Effect size corresponding to positive values (=red) indicates that Controls present a larger value of the given parameter, that corresponding to negative ones (=blue) indicates that Controls have a smaller value.

Movies S1-S8 shows the corresponding animations using both bullseye representation and a 3D representation in three different views where selected landmarks are evidenced on the general endocardial surface. The parameters that contribute more to the 400 landmarks final selection are the radial and longitudinal strains all around the apical part. These 400 landmarks are also depicted in Fig. 4 where shapes explained by high and low values of the first three PC scores coming from shape analysis are illustrated.

3. Parallel Transport and modern shape analysis

Results of shape analysis show that the selected regions of Controls and G+LVH- have trajectories which are very different.

The first three PC scores explain collectively 71.9% of total Variance (PC1: 60.2%; PC2: 6.14%; PC3: 5.6%). Under parametric Tukey post-hoc test, the PC1-PC3 angle significantly differs between Controls and HCM (p-value: 0.023) while it is marginally non-significant for Controls-G+LVH- comparison (p-value: 0.06). Permutated MANOVA indicates that Controls' trajectory shape significantly differs from that of the other two categories (Controls-G+LVH- p- value: 0.029; Controls-HCM p-value: 0.001). Notably, Tukey test indicates that G+LVH- trajectory' size is considerably smaller than that of Controls (p-value: 0.003, Cohen'd effect size: 1.12). PC1 direction is dictated by the systo-diastolic difference; along this axis Controls occupy more variance than both G+LVH- and HCM.

At positive PC1 values (i.e. systole) the pure LV shape becomes more elongated and the apex bends toward basal- septal direction. G+LVH- and HCM, instead, are more dispersed, relative to Controls, along PC3. Animations of the global mean shape changes at all homologous times for the three categories and along PC1

and PC3 are shown in Movies S9-S11. Fig. 5 shows the course of the PC1-PC2-PC3 when evaluated at each homologous time for each category. PC1 suggests that G+LVH-always sets apart from Controls. In end-systole (homologous time 5) and proto- diastole (=the very beginning of diastole; homologous times 6-9), in particular, they are placed close to HCM. The same happens along PC3, while for PC2 the signal is weaker.

4. Machine learning for G+LVH- recognition

Table 3 shows classification results relative to classic 3D STE variables evaluated from diastole at all homologous times and selected according to feature's selection procedure described in Methods. Radial and Circumferential strains are the most represented parameters. The former is mainly represented on the mid-segments, the latter on the apical ones. Longitudinal strain is represented on two apical segments. The best classification performances are for global Circumferential strain but do not seem very effective in recognizing G+LVH- condition. This could be due to the fact that tele-diastolic states (=the final stages of diastolic phase) are not properly quantified using classic 3D STE approach.

TABLE 3. Classic 3D STE parameters selected according to feature's selection procedure. The selected homologous times have absolute Cohen'd > 1.

STE parameters	Accuracy	Specificity	Sensitivity	AUC	Selected homologous times
Strain_BS	0.499	0.498	0.527	0.601	3
RStrain_MAS	0.588	0.589	0.557	0.641	2 3 4 5 6
RStrain_MS	0.694	0.699	0.584	0.720	5 6 7 8 9 13 14
RStrain_global	0.522	0.521	0.561	0.629	4 5 6 7 8 9
CStrain_BI	0.612	0.611	0.648	0.707	13 14 15
CStrain_BP	0.600	0.601	0.588	0.657	12 13 14
CStrain_MS	0.690	0.695	0.576	0.712	7 8 9 10 12 13
CStrain_ML	0.610	0.615	0.496	0.635	3 4 5 6 7 8 9
CStrain_AA	0.630	0.628	0.678	0.701	3 4 5 6 7 8 9
CStrain_AS	0.680	0.688	0.501	0.666	3 4 5 6 7 8 9 10
CStrain_AI	0.568	0.568	0.587	0.643	3 4 5 6 7 8 9
CStrain_AL	0.686	0.692	0.522	0.665	4 5 6
CStrain_global	0.677	0.676	0.706	0.775	4 5 6 7 8 9 10 12 13 14
LStrain_AI	0.635	0.634	0.664	0.719	3 4 5 6 7 8 12

LStrain_AL	0.637	0.633	0.716	0.731	3 4

Features selection performed on first six PC scores coming from shape analysis evaluated at all homologous times with significant absolute Cohen'd> 1 returned 24 predictors specified in Fig. 6. PC1 is represented nearly in its entirety followed by PC3 and PC5, respectively. Using solely Controls/G+LVH- as dependent binary variable, the permuted SVM returned results shown in Table 4. Even varying the hyper-parameter C, we found very good classification performances (in terms of mean and medians of the 1000 simulated classification exercises) with AUC close to 0.9 and total accuracy slightly smaller than 0.8. Sensitivity is particularly high with C=0.1.

TABLE 4. Permutated SVM results.

Diagnostic parameter	**Mean**	**Median**	**Normality test *p*-value**	**Bootstrap 95% median C.I.**
C=0.1				
AUC	0.910	0.914	3.8e-11	(0.91, 0.92)
Specificity	0.752	0.757	2.2e-16	(0.754, 0.759)
Sensitivity	0.959	1	2.2e-16	not applicable
Total Accuracy	0.761	0.766	2.2e-16	(0.765, 0.767)
C=25				
AUC	0.887	0.905	2.2e-16	(0.901, 0.910)
Specificity	0.784	0.783	2.2e-16	(0.767, 0.791)
Sensitivity	0.829	1	2.2e-16	not applicable
Total Accuracy	0.786	0.792	2.2e-16	(0.789, 0.795)
C=100				
AUC	0.881	0.905	2.2e-16	(0.901, 0.913)
Specificity	0.781	0.784	2.2e-16	(0.767, 0.792)
Sensitivity	0.829	1	2.2e-16	not applicable
Total Accuracy	0.783	0.792	2.2e-16	(0.791, 0.793)

7. DISCUSSION AND CONCLUSION

The results obtained in this study suggest that, if properly handled, 3D STE coupled with modern shape analysis might unveil G+LVH- condition with high accuracy. Initially, 3D STE can be effectively used to select shape subdomains to be further analyzed with Parallel Transport and machine learning. However, this should be done at the level of each single landmark and not at that of AHA segments. This permits to treat the landmark cloud in a quasi-continuous fashion and to subdivide initial topology into the best sub-configuration to discriminate Controls from G+LVH- during deformation analysis. As stated earlier, 3DSTE alone has not been very effective in associating G+ condition on the basis of solely phenotypic features as also demonstrated by Table 3.

Recently, calibrated integrated backscatter (cIBS), combined with anteroseptal Longitudinal strain, proved quite effective in recognizing G+LVH- (Yu et al., 2012). It was shown there that G+LVH- patients had an increased cIBS of the basal antero-septal region as compared to controls, suggesting substantial myocardial structural alterations. Noteworthy however, Longitudinal strain was computed in 2D. On the other hand, CMR allowed to explore peculiar attributes able to identify with good accuracy G+LVH-: myocardial crypts, anterior mitral valve lea et elongation, increased LV apical trabecular complexity (measured via Fractal Dimension) and smaller LV systolic cavity. Previously (Reant et al., 2015) septal convexity measured from CMR in apical 4-chamber view was claimed to be prognostic of G+LVH- condition. These features are, however, not directly linked to the deformation/motion along an entire heart cycle. Different phenotypes could deform, in fact, in similar way and vice versa.

A very interesting connection between the present study and previous investigations could be that between the sub-configuration we selected here on the basis of 3D STE strains analysis, plus modern shape analysis and the fact that, using CMR, some authors found that the Fractal Dimension of trabeculae carneae is significantly higher in G+LVH- relative to Controls just on the apical part (Captur et al., 2014b). They hypothesized that this could be due to the irregular expression of mutated sarcomeric genes that act in adults as during gestation time in healthy subjects. This augmented “hypercomplexification” (Captur, Karperien, Hughes, Francis & Moon, 2016) has not been discussed previously in terms of possible mechanical impairments of that part of LV affected by hypertrabeculation. A recent study focused on LV hypertrophy faced the mechanical effects of apical hypertrabeculation and trabecular cutting using both ex vivo and simulated experiments. (Halaney et al., 2017). It was found that hypertrabeculation of pathological subjects implies a reduced LV compliance during diastolic phase.

On the opposite, experimental trabecular apical cutting, or its reduction on the simulated data, confirmed that diastolic compliance is significantly improved. It is highly suggestive that our selected sub-configuration involves just the apical region where an augmented trabecular complexity was observed in G+LVH-. Moreover, our sub-configuration clearly shows, looking at Movies S10 and S11, that G+LVH- and HCM present a much less "dilated" morphology in diastole. This can be interpreted as a reduced compliance during diastolic phase putting a translational thread on the results presented here which are perfectly in line with modelling, experiments and different methodological 3D approaches to the study of G+LVH- condition (Captur et al., 2014a; Captur, Karperien, Hughes, Francis & Moon, 2016; Halaney et al., 2017). We then speculate that our

results represent an important corroboration, made upon pure shape and deformation analysis, of evidences previously found using different methods and approaches.

In addition, Fig. 5 shows that PC1, which dictates systo-diastolic direction, presents the larger effect size between Controls and G+LVH- just around diastolic phase (homologous time 2). This is certainly not seen using classic 3D STE parameters as they consider diastole as a reference and values approaching to diastole gradually tend to zero. Our approach not only considers diastole as a deformed state, but also can compare cohort's means during the entire cycle by exploiting the homologous times scheme which is fundamental for this purpose. This opens to a rationale to be applied in common clinical practice. Clinicians, in fact, may not have the possibility (in terms of time and computational skills) to perform rapidly all computational steps presented in this study.

We then hypothesize a 3D STE echocardiographic device that incorporates them during acquisition. All computational steps can be done internally to the device and the statistics are performed using previously recorded databases (or even publicly available databases that could be loaded using an internet connection) that are used for learning and then for classifying a new subject. Once the clip is acquired, the operator is asked to input the millisecond corresponding to the four strictly homologous times shown in Fig. 2. Then, all phases we described till now can be easily completed by the device. Of course the public database could include additional parameters not considered here of both echocardiographic and non echocardiographic nature: cIBS, septal convexity measure, number of crypts (if CMR is available), etc. This will certainly improve the classification accuracy. All this is not di cult to achieve if one or more vendors agree in building the 3D STE databases which, given that 3D topology is vendor dependent, will be inevitably vendor specific. The existence of this global database produced by the contribution of multiple centers will ease also the evaluation of inter-operator dependence at two levels: the one of image acquisition and that of 3D reconstruction. This could open a new era for the interrelationship between basic research and common clinical applications. Moreover, the production of large 3D STE databases will contribute to the pathophysiological understanding of a large number of diseases (not only those studied here), thus easing the diagnosis of incumbent pathology and the management of patients. In absence of these publicly available databases, we share the data described in this study upon request.

This study has the main limitation that G+LVH- cohort is represented by only 11 subjects. Thus, we used 8 Control and 8 G+LVH- subjects in 1000-fold permuted SVM. The genetic status, moreover, was not blind to the operator during the 3D echo screening. While the Control sample is relatively large, a study including a larger G+LVH- cohort could corroborate the findings of our investigation. As a consequence, we neither tested for deformational behavior of different sarcomeric gene mutations. Moreover, 3D STE parameters were evaluated in systole for sub-selecting landmarks; this could be not mandatory and more homologous times could enter the procedure. Finally, it is single center in design and G+LVH- and HCM patients were inter-related.

Acknowledgements

The authors wish to express their gratitude to Willem Gorissen, Clinical Market Manager Cardiac Ultrasound at Toshiba Medical Systems Europe, Zoetermeer, The Netherland, for continuous support and help. Author

contributions: C.T., P.N., A.M., L.T., and M.S. conceived the study; C.T., A.E., G.E., F.R. and C.C. acquired the data; P.P., P.E.P., V.V. per- formed the statistical analyses; P.P., L.T. and P.E.P. wrote the paper. All authors reviewed the manuscript and provided meaningful intellectual contributions. Data and materials availability: All datasets are available upon request to the corresponding author (PP).

Conflict of interest

The authors declare that they have no competing interests.

Funding

The authors acknowledge the Financial support of Sapienza, Università di Roma, Italy, for the Sapienza Grant # AI2617PT9LE (2017) "Mechanics of soft fibered active materials", and of the Italian Group of Mathematical Physics (GNFM-INdAM).

References

Aly, M.F.A., Brouwer, W.P., Kleijn, S.A., van Rossum, A.C., Kamp, O. (2014). Three-dimensional speckle tracking echocardiography for the preclinical diagnosis of hypertrophic cardiomyopathy. *The International Journal of Cardiovascular Imaging, 30,* 523-533. 10.1007/s10554-014-0364-5

Baeßler, B., Mannil, M., Maintz, D., Alkadhi, H., & Manka, R. (2018). Texture analysis and machine learning of non-contrast T1-weighted MR images in patients with hypertrophic cardiomyopathy. Preliminary results. *European Journal of Radiology*, *102*, 61- 67. 10.1016/j.ejrad.2018.03.013

Captur, G., Karperien, A.L., Hughes, A.D., Francis, D.P., & Moon, JC.(2016). The fractal heart - embracing mathematics in the cardiology clinic. *Nature Reviews Cardiology, 14,* 56-64. 10.1038/nrcardio.2016.161

Captur, G., Lopes, L.R., Mohun, T.J., Patel, V., Li, C., Bassett, P., ... Moon, J. C. (2014a). Prediction of Sarcomere Mutations in Subclinical Hypertrophic Cardiomyopathy. *Circulation: Cardiovascular Imaging, 7,* 863-871. 10.1161/CIRCIMAGING.114.002411

Captur, G., Lopes, L.R., Patel, V., Li, C., Bassett, P., Syrris, P., ...Moon, J.C. (2014b). Abnormal Cardiac Formation in Hypertrophic Cardiomyopathy. *Circulation: Cardiovascular Genetics, 7,* 241-248. https://doi.org/10.1161/CIRCGENETICS.113.000362

De, S., Borowski, A.G., Wang, H., Nye, L., Xin, B., Thomas, J.D., ...Tang, W.H. (2011). Subclinical echocardiographic abnormalities in phenotype-negative carriers of myosin-binding protein C3 gene mutation for hypertrophic cardiomyopathy. *American Heart Journal, 162,* 262-267.e.3. 10.1016/j.ahj.2011.05.018

Gray, B., Ingles, J., & Semsarian, C. (2011). Natural history of genotype positive–phenotype negative patients with hypertrophic cardiomyopathy. *International Journal of Cardiology*,152, 258–259. 10.1016/j.ijcard.2011.07.095

Haland, T.F., Hasselberg, N.E., Almaas, V.M., Dejgaard, L.A., Saberniak, J., Leren, I.S., ... Edvardsen, T. (2017). The systolic paradox in hypertrophic cardiomyopathy. *Open Heart*, *4*, e000571. 10.1136/openhrt-2016-000571

Halaney, D.L., Sanyal, A., Nafissi NA, Escobedo D, Goros M, Michalek J, ... Han, H. C. (2017). The Effect of trabeculae carneae on left ventricular diastolic compliance: improvement in compliance with trabecular cutting. *Journal of Biomechanical Engineering, 139,* 031012. 10.1115/1.4035585

Karatzoglou, A., Smola, A., Hornik, K., & Zeileis, A. (2004). Kernlab - An S4 Package for Kernel Methods in R. *Journal of Statistical Software, 11,* 1-20. 10.18637/jss.v011.i09

Kauer, F., van Dalen, B.M., Michels, M., Schinkel, A.F.L., Vletter, W.B., van Slegtenhorst, M.,... Geleijnse, M,L. (2017). Delayed and decreased LV untwist and unstrain rate in mutation carriers for hypertrophic cardiomyopathy. *European Heart Journal Cardiovascular Imaging*, *18*, 383-389. 10.1093/ehjci/jew213

Madeo, A., Piras, P., Re, F., Gabriele, S., Nardinocchi, P., Teresi, L., … Puddu, P.E. (2015). A New 4D Trajectory-Based Approach Unveils Abnormal LV Revolution Dynamics in Hypertrophic Cardiomyopathy. *PLosOne, 4,* e0122376.

Maiorino L., Farke AA., Kotsakis T. &Piras P. (2013). Is *Torosaurus Triceratops*? Geometric morphometric evidence of late Maastrichtian ceratopsid dinosaurs. *PLosONE, 8, ISSN*: 1932-6203. 10.1371/journal.pone.0081608.

Maron, B.J., & Maron, M.S.(2013). Hypertrophic cardiomyopathy. *The Lancet, 381*, 242-255. https://doi.org/10.1016/S0140-6736(12)60397-3

Maron, B.J., & Semsarian, C. (2010). Emergence of gene mutation carriers and the expanding disease spectrum of hypertrophic cardiomyopathy. *European Heart Journal, 31,* 1551-1553. 10.1093/eurheartj/ehq111

Maron, B.J., Ommen, S.R., Semsarian, C., Spirito, P., Olivotto, I., & Maron, MS. (2014). Hypertrophic Cardiomyopathy. *Journal of the American College of Cardiology, 64,* 83-99. 10.1016/j.jacc.2014.05.003

Maron, B.J., Yeates, L., & Semsarian, C. (2011). Clinical Challenges of Genotype Positive (+) Phenotype Negative (-) Family Members in Hypertrophic Cardiomyopathy. *The American Journal of Cardiology*, *107*, 604-608. 10.1016/j.amjcard.2010.10.022

Maron, M.S., Rowin, E.J., Lin, D., Appelbaum, E., Chan, R.H., Gibson, C.M., … (2012).. Prevalence and Clinical Profile of Myocardial Crypts in Hypertrophic Cardiomyopathy. *Circulation: Cardiovascular Imaging, 5,* 441-447. 10.1161/CIRCIMAGING.112.972760

Piras P., Teresi L., Buscalioni A.D. & Cubo J. (2009).The shadow of forgotten ancestors differently constrains the fate of Alligatoroidea and Crocodyloidea. *Global Ecology and Biogeography, 18*, 30-40. 10.1111/j.1466-8238.2008.00426.x.

Piras P., Buscalioni A.D., Teresi L., Raia P., Sansalone G., Kotsakis T. & Cubo J. (2014). Morphological integration and functional modularity in the crocodilian skull. *Integrative Zoology, 9*, 498-516. 10.1111/1749-4877.12062.

Piras, P., Torromeo, C., Re, F., Evangelista, A., Gabriele, S., Esposito, G., … Puddu, P.E. (2016). Left Atrial trajectory impairment in Hypertrophic Cardiomyopathy disclosed by Geometric Morphometrics and Parallel Transport. *Scientific Reports , 6,* 34906. 10.1038/srep34906

Piras, P., Teresi, L., Puddu, P.E., Torromeo, C., Young, A.A., Suinesiaputra, A., … , Medrano-Gracia, P. (2017a). Morphologically normalized left ventricular motion indicators from MRI feature tracking characterize myocardial infarction. *Scientific Reports*, 7, 12259. 10.1038/s41598-017-12539-5

Piras, P., Torromeo, C., Evangelista, A., Gabriele, S., Esposito, G., Nardinocchi, P., … Puddu, P.E. (2017b). Homeostatic Left Heart integration and disintegration links atrio-ventricular covariation's dyshomeostasis in Hypertrophic Cardiomyopathy. *Scientific Reports, 7*, 6257. https://doi.org/10.1038/s41598-017-06189-w

Prabhakar, R., Boivin, G.P., Grupp, I.L., Hoit, B., Arteaga, G., Solaro, J.R., ... Wieczorek, D.F. (2001). A Familial Hypertrophic Cardiomyopathy α -Tropomyosin Mutation Causes Severe Cardiac Hypertrophy and Death in Mice. *Journal of Molecular and Cellular Cardiology, 33*, 1815-1828. 10.1161/01.RES.88.4.383

Reant, P., Captur, G., Mirabel, M., Nasis, A., Sado, D.M., Maestrini, V., ... Moon, J.C. (2015). Abnormal septal convexity into the left ventricle occurs in subclinical hypertrophic cardiomyopathy. *Journal of Cardiovascular Magnetic Resonance, 17,* 64. https://doi.org/10.1186/s12968-015-0160-y

Sawilowsky, S.S. (2001). New Effect Size Rules of Thumb. *Journal of Modern Applied Statistical Methods, 8,* 597-599. 10.22237/jmasm/1257035100

Schofield, R., Ganeshan, B., Kozor, R., Nasis, A., Endozo, R., Groves, A., … Moon, J.C. (2016). CMR myocardial texture analysis tracks di er- ent etiologies of left ventricular hypertrophy. *Journal of Cardiovascular Magnetic Resonance, 18,* S1-O82. https://doi.org/10.1186/1532-429X-18-S1-O82

Torricelli, F., Girolami, F., Olivotto, I., Passerini I, Frusconi S, Vargiu D, ... Cecchi F. (2003). Prevalence and clinical profile of troponin T mutations among patients with hypertrophic cardiomyopathy in Tuscany. *American Journal of Cardiology, 92,* 1358-1362. https://doi.org/10.1016/j.amjcard.2003.08.031

Varano, V., Gabriele, S., Teresi, L., Dryden, I.L., Puddu, P.E., Torromeo, C., … Piras, P. (2017). The TPS Direct Transport: A New Method for Transporting Deformations in the Size-and-Shape Space. *International Journal of Computer Vision, 124,* 384-408. https://doi.org/10.1007/s11263-017-1031-9

Xiao, W., & Oefner, P.J. (2001). Denaturing high-performance liquid chromatography: a review. *Human Mutation, 17,* 439-474. 10.2353/jmoldx.2006.050098

Yiu, K.H., Atsma, D.E., Delgado, V., Ng, A.C.T., Witkowski, T.G., Ewe, S.H., … Marsan, N.A. (2012). Myocardial Structural Alteration and Systolic Dysfunction in Preclinical Hypertrophic Cardiomyopathy Mutation Carriers. *PLoSONE*, *7*, e36115. https://doi.org/10.1371/journal.pone.0036115

Yu, B., Sawyer, N.A., Caramins, M., Yuan, Z.G., Saunderson, R.B., …Trent, RJ. (2005). Denaturing high performance liquid chromatography: high throughput mutation screening in familial hypertrophic cardiomyopathy and SNP genotyping in motor neurone disease. *Journal of Clinical Pathology, 58,* 479-485. 10.1136/jcp.2004.021642

Figure Captions

FIGURE 1. Top panels: Geometry of the LV as sampled by the landmarks tracked with the 3D echocardiographic device. A) Actual geometry of LV; black and red landmarks represent the epicardial and the endocardial layer, respectively. B) Bullseye plot showing the landmarks position with respect to the AHA segments. Bottom panels: Bullseye of the mean radial strain represented with reference to the AHA segments. C) Mean values for each segment. D) Point-wise values. Inset D shows the names the AHA segments, oriented according to the Toshiba Artida format and that the region with maximum strain (identified by dotted lines) is localized between two segments, a finding which cannot be inferred from the bullseye plot at left.

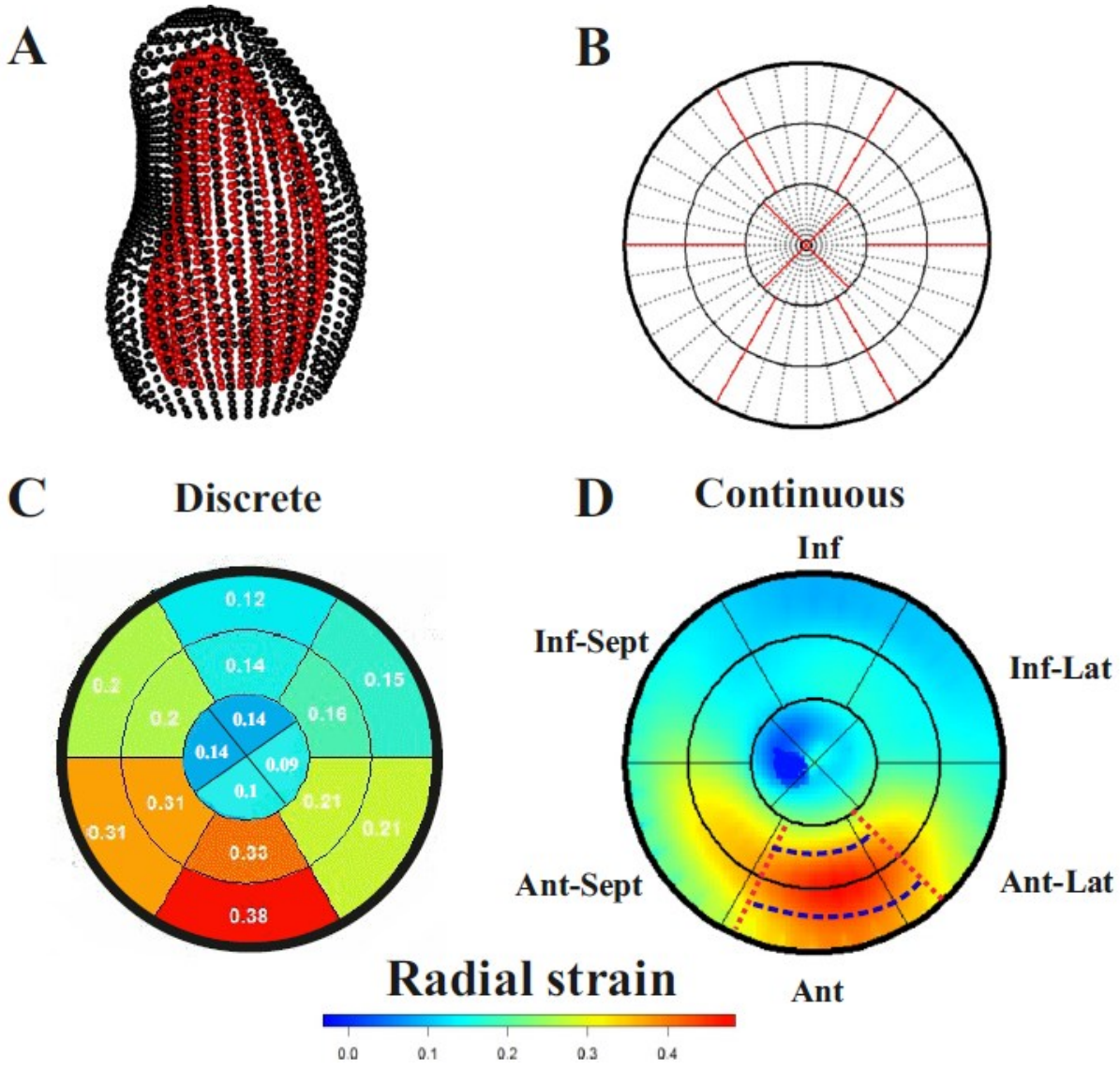

FIGURE 2. Selection of the homologous times. Top: On the Time-Volume plot we report the acquired frames (circle), the 4 primal times (triangle), and the additional, equally-spaced, times (large circle). Bottom: ECG trace used to select the electrical events.

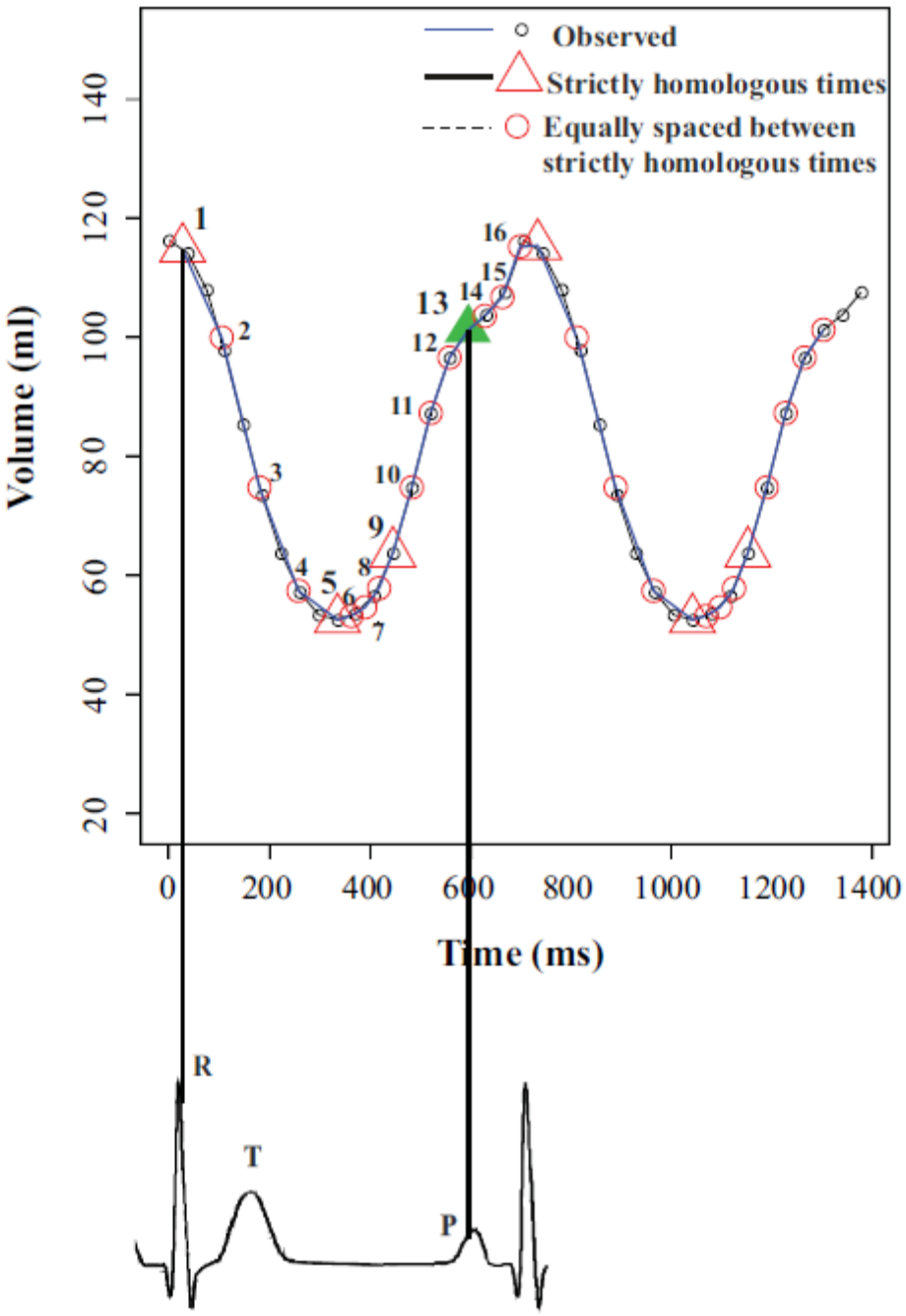

FIGURE 3. The course of the first three PC scores evaluated at all homologous times. Tick labels indicate the pairwise comparisons (1=Control, 2=G+LVH-, 3=HCM) that significantly differ (at 0.05 level of significance) for each parameter under ANOVA.

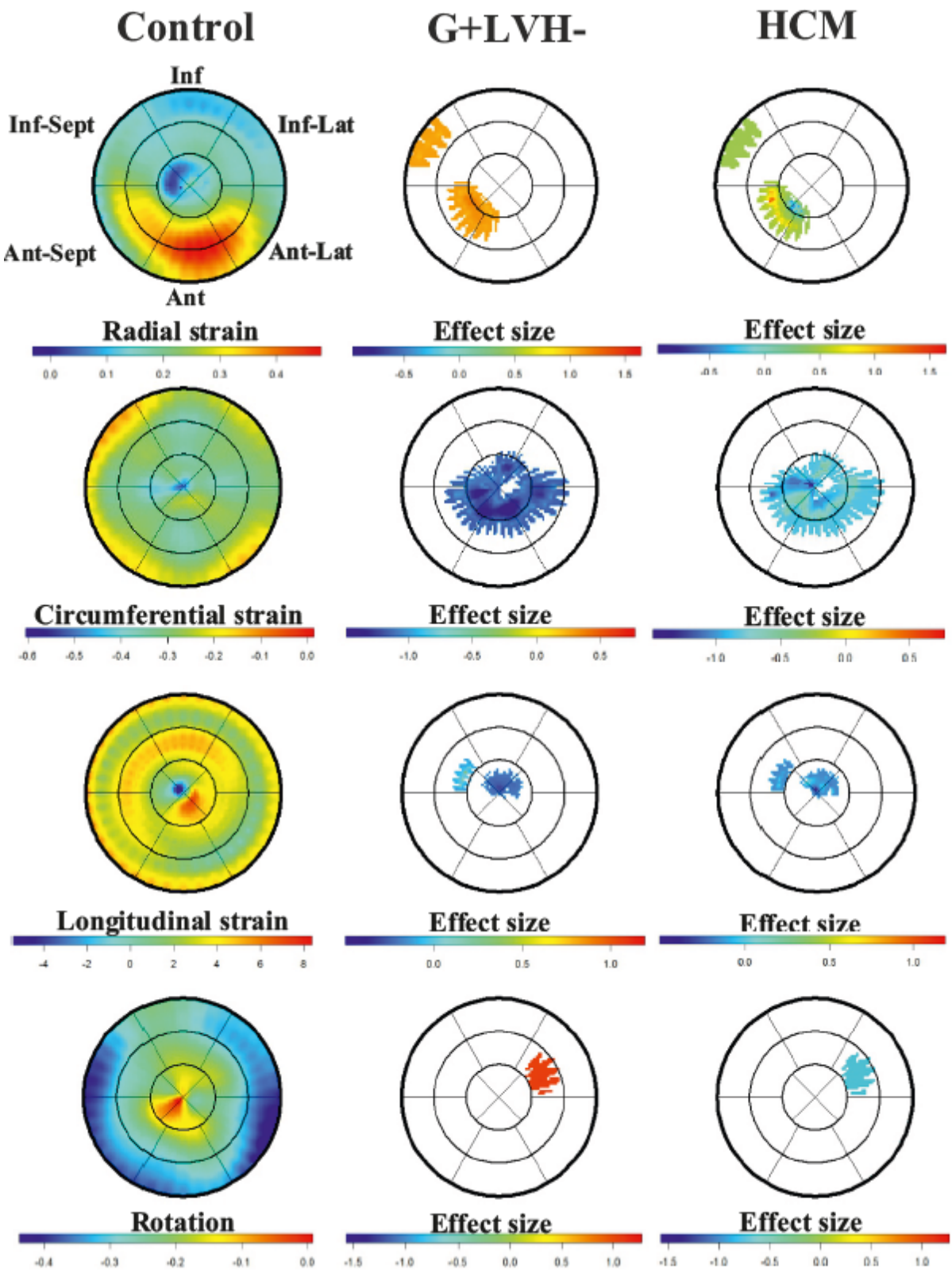

FIGURE 4. Selected features for SVM classification procedure. Tick labels indicate the pairwise comparisons (among Control, G+LVH- and HCM) that significantly differ (1=Control, 2=G+LVH-, 3=HCM) for each parameter under ANOVA.

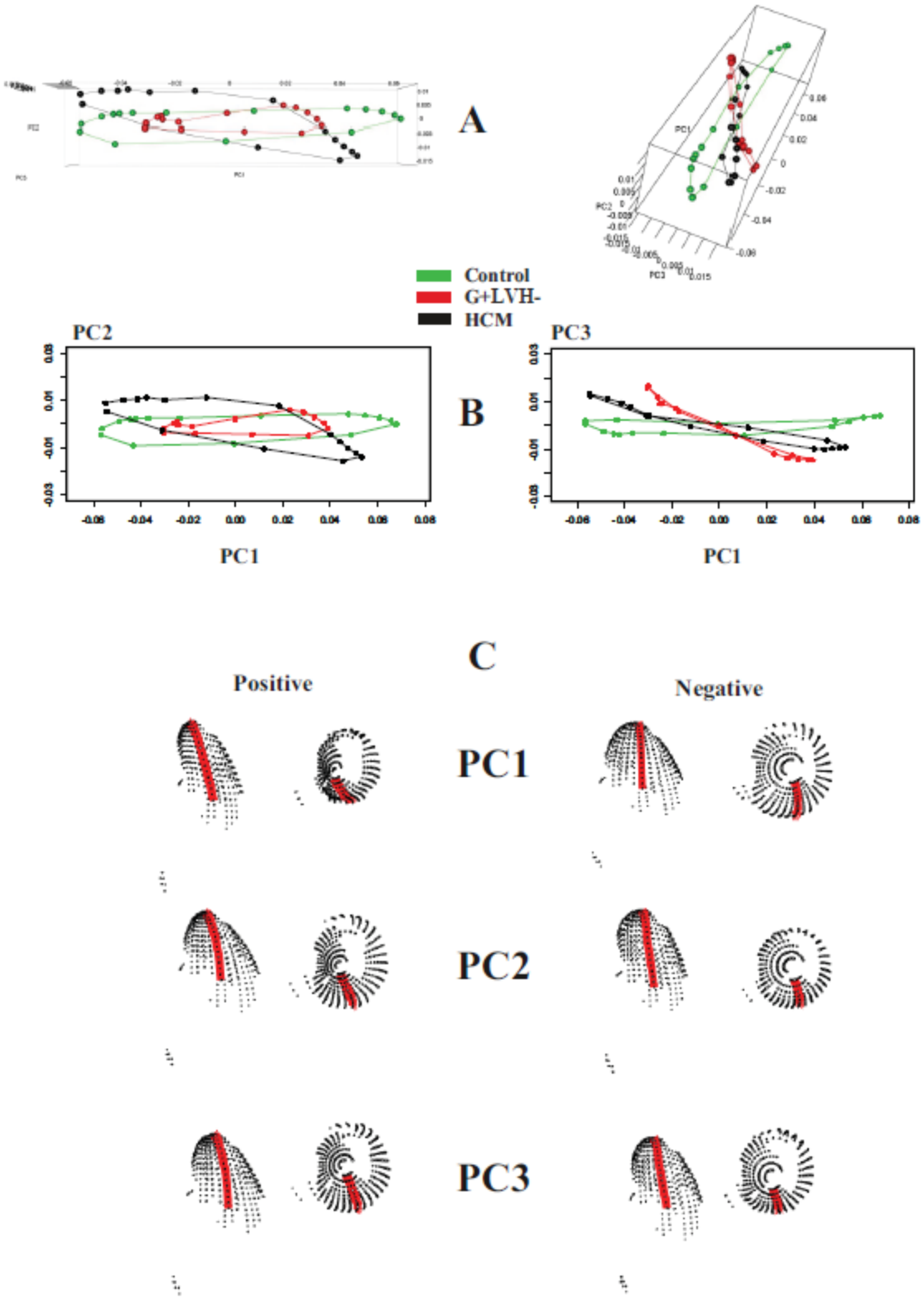

FIGURE 5. Bullseye representation of the four 3D STE parameters evaluated in systole for cohorts. Only selected landmarks (i.e. those significant under ANOVA and with an absolute Cohen'd e ect size >1 in Controls/G+LVH- comparison) are depicted, while the others have been shut o . For sake of visualization we interpolated the white space between landmarks on the bullseye circular domain using kriging geostatistical technique. While for Controls we show the mean parameter value, for G+LVH- and HCM we show the Cohen'd effect size. Positive effect size (=red) indicates that Controls presents a larger value of the given parameter, negative effect size (=blue) indicates that Controls have a smaller value.

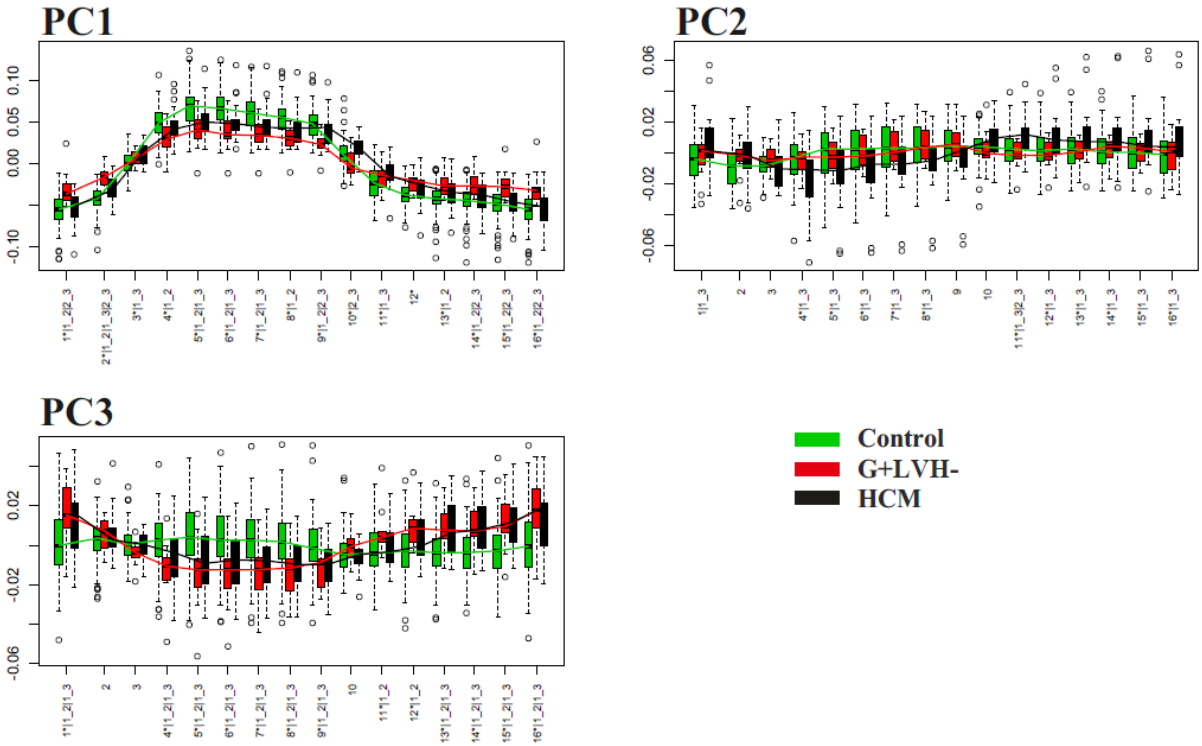

FIGURE 6. Results of modern shape analysis. (A) Per-group mean trajectories in the three dimensional space of the first 3 PC scores. (B) PC1-PC2 and PC1-PC3 scatterplots. (C) Shapes corresponding to positive and negative extremes of the first three PCs cores; both lateral and apical views are illustrated. Red line indicates the approximate position of interventricular septum.